

HOSTED BY

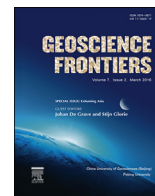


ELSEVIER

Contents lists available at ScienceDirect

China University of Geosciences (Beijing)

Geoscience Frontiers

journal homepage: www.elsevier.com/locate/gsf

Focus paper

Contrasted continental rifting via plume-craton interaction: Applications to Central East African Rift



Alexander Koptev^{a,*}, Evgueni Burov^a, Eric Calais^b, Sylvie Leroy^a, Taras Gerya^c, Laurent Guillou-Frottier^d, Sierd Cloetingh^e

^a Sorbonne Universités, UPMC Univ Paris 06, CNRS, Institut des Sciences de la Terre de Paris (iSTeP), 4 place Jussieu 75005 Paris, France

^b Ecole Normale Supérieure, Department of Geosciences, PSL Research University, CNRS UMR 8538, Paris, France

^c ETH-Zurich, Institute of Geophysics, Sonnegstrasse 5, Zurich, Switzerland

^d BRGM, Georesources Division, Orléans, France

^e Utrecht University, Netherlands

ARTICLE INFO

Article history:

Received 21 August 2015

Received in revised form

2 November 2015

Accepted 5 November 2015

Available online 30 November 2015

Keywords:

Plume-lithosphere interaction

Continental rifting

East African Rift System

3D numerical modeling

ABSTRACT

The East African Rift system (EARS) provides a unique system with the juxtaposition of two contrasting yet simultaneously formed rift branches, the eastern, magma-rich, and the western, magma-poor, on either sides of the old thick Tanzanian craton embedded in a younger lithosphere. Data on the pre-rift, syn-rift and post-rift far-field volcanic and tectonic activity show that the EARS formed in the context of the interaction between a deep mantle plume and a horizontally and vertically heterogeneous lithosphere under far-field tectonic extension. We bring quantitative insights into this evolution by implementing high-resolution 3D thermo-mechanical numerical deformation models of a lithosphere of realistic rheology. The models focus on the central part of the EARS. We explore scenarios of plume-lithosphere interaction with plumes of various size and initial position rising beneath a tectonically pre-stretched lithosphere. We test the impact of the inherited rheological discontinuities (suture zones) along the craton borders, of the rheological structure, of lithosphere plate thickness variations, and of physical and mechanical contrasts between the craton and the embedding lithosphere. Our experiments indicate that the ascending plume material is deflected by the cratonic keel and preferentially channeled along one of its sides, leading to the formation of a large rift zone along the eastern side of the craton, with significant magmatic activity and substantial melt amount derived from the mantle plume material. We show that the observed asymmetry of the central EARS, with coeval amagmatic (western) and magmatic (eastern) branches, can be explained by the splitting of warm material rising from a broad plume head whose initial position is slightly shifted to the eastern side of the craton. In that case, neither a mechanical weakness of the contact between the craton and the embedding lithosphere nor the presence of second plume are required to produce simulations that match observations. This result reconciles the passive and active rift models and demonstrates the possibility of development of both magmatic and amagmatic rifts in identical geotectonic environments.

© 2015, China University of Geosciences (Beijing) and Peking University. Production and hosting by Elsevier B.V. This is an open access article under the CC BY-NC-ND license (<http://creativecommons.org/licenses/by-nc-nd/4.0/>).

1. Introduction

Rifting of continental lithosphere is a fundamental geodynamic process that controls the growth and evolution of continents and the birth of ocean basins (e.g., Buck, 1991, 2007). It involves the entire

mantle-lithosphere system through heat transfer, active or passive mantle flow and magmatism, stretching and thinning of the crust/upper mantle due to far-field forces, and, possibly, viscous coupling between mantle flow and lithospheric deformation. In the active or plume scenario, rifting occurs as a result of dynamic stresses imparted by large mantle diapirs or sheet-like mantle upwelling, rising through the mantle, that advect sufficient heat to produce large amounts of surface volcanism (Sengör and Burke, 1978). In the passive or plate scenario, rifting occurs as a result of tensional intra-plate far-field forces transmitted within lithospheric plates, while

* Corresponding author.

E-mail address: alexander.koptev@upmc.fr (A. Koptev).

Peer-review under responsibility of China University of Geosciences (Beijing).

mantle upwelling and melting is a consequence of lithospheric stretching (McKenzie, 1978). At oceanic spreading centers the major driving mechanism is mantle upwelling. However, ridge push forces associated with mantle upwelling and near ridge topographic gradients are either initially smaller or become progressively smaller than the far-field forces associated with slab pull of the subducting lithosphere (Olson et al., 2001). Hence, at large scales, even oceanic rifting would be impossible without far-field forces driving mature oceanic lithosphere away from the ridge, thus allowing for continuous creation of space for the accretion of new lithosphere. In continents, rifting and passive margin development concepts and models are based on the so-called “passive rifting” mechanism where mantle upwellings are not playing a significant role in rift dynamics (Buck, 1991; Burov and Poliakov, 2001; Whitmarsh et al., 2001; Huismans and Beaumont, 2003; Buck, 2007; Cloetingh et al., 2013; Burov et al., 2014). However, it is generally accepted that some continental rifts, such as the Afar and Central Africa rift regions (Ritsema et al., 1999; Nyblade et al., 2000) or the Rio Grande system (Satsukawa et al., 2011) involve significant mantle contribution. The dynamic contribution of large mantle upwellings in other continental rifts such as Baikal (e.g., Burov et al., 1994; Petit et al., 1997), the Rhine graben, or the Pannonian basin (e.g., Cloetingh et al., 1999) is still debated due to the absence of the records of magmatic pre-rift activity and clear seismological signatures of deeply-rooted mantle upwellings. However, while the observational signature of mantle-induced rifting is often equivocal, a purely passive mechanism also meets a number of problems, specifically in zones of ultra-slow rifting. This issue was termed the “tectonic force paradox”, which states that far-field tectonic forces transmitted in the lithosphere are not sufficient to rupture normal continental lithosphere, unless it is previously weakened (e.g., Behn et al., 2006; Buck, 2006, 2007). Indeed, simple estimation of the forces needed to extend lithosphere (Buck, 2006) shows that for reasonable driving force levels ($5 \times 10^{12} \text{ N m}^{-1}$), only extremely thin lithosphere ($<30 \text{ km}$) can be rifted tectonically in absence of magmatic dyke intrusion. Hence, it is often suggested that continental rifting and breakup either require meso-scale strain softening (Behn et al., 2006; Buck, 2007; Huismans and Beaumont, 2007; Precigout et al., 2007) or additional strain localization mechanisms associated, for example, with the interactions between mantle plume and the overlying lithosphere (Burov et al., 2007; Burov and Gerya, 2014; Koptev et al., 2015; Stamps et al., 2015).

The role of mantle upwellings in continental rift dynamics is a long debated topic, illustrated by the classic “passive versus active” rifting debate (Fitton, 1983; Foulger et al., 2000; Foulger and Hamilton, 2014). Seismic tomography reveals deep-seated low-velocity anomalies in the mantle underneath several rift zones (e.g., Ritsema et al., 1999; Nyblade et al., 2000; Nolet et al., 2006, 2007) that cannot be interpreted as a consequence of passive lithospheric stretching. In particular, broad low seismic velocity zones observed throughout the upper mantle cannot be easily inferred from small-scale mantle convection induced by passive stretching of the lithosphere, for example in the East African (Ritsema et al., 1999; Nyblade et al., 2000; Adams et al., 2012) or Rio Grande (Satsukawa et al., 2011) rift systems. Evidence for strain accommodation by magma intrusion in young continental rift basins (Calais et al., 2008) is also indicative of magma-assisted rifting (Kendall et al., 2005, 2006). Finally, the EARS shows petrological evidence for pervasive elevated mantle temperature under the rift requires significant heating from below and/or fluid-assisted melting (Rooney et al., 2012; Ferguson et al., 2013; Armitage et al., 2015). These observations are indicative of a contribution of deep mantle processes in the evolution some continental rifts, in particular the EARS.

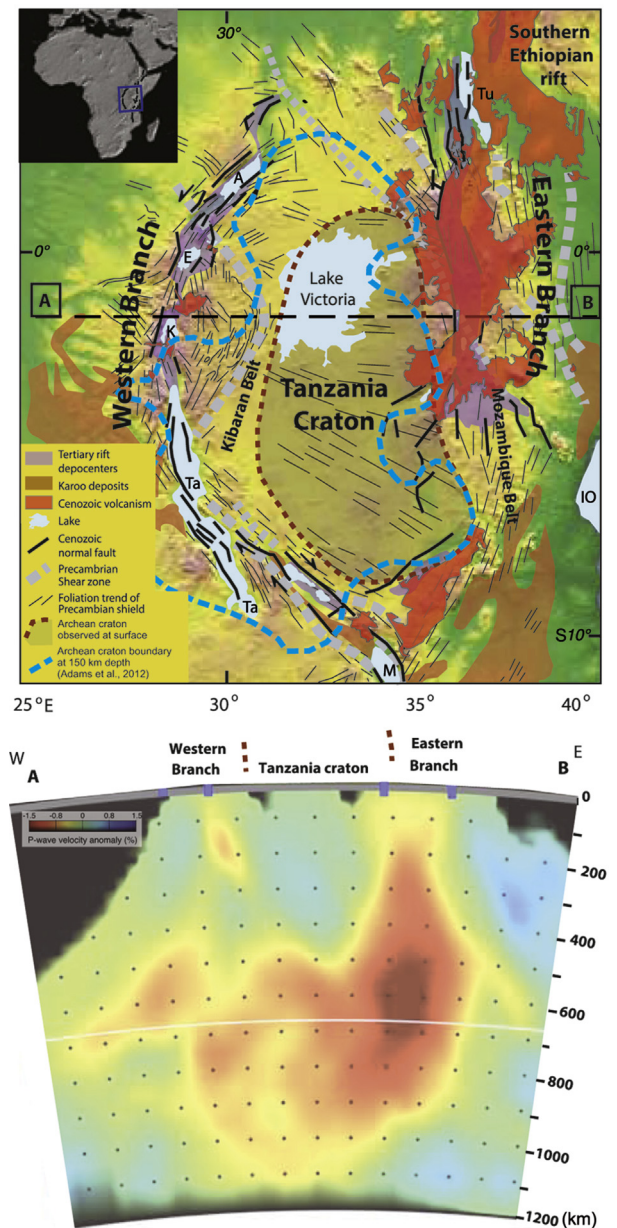


Figure 1. Geological and geophysical context. Top: Geological map of the EARS showing the surface extent of the Tanzanian craton, surrounded on both sides by active rift branches – the magma-poor western rift characterized by low-volume volcanic activity, large ($M > 6.5$) magnitude earthquakes, and hypocenters at depths up to 30–40 km, while the magma-rich eastern rift is characterized by a broad zone of shallow (5–15 km) and smaller magnitude seismicity, but voluminous Cenozoic volcanism. Note the geometry (dashed line) of the craton boundary at 150 km depth (Adams et al., 2012). Bottom: E–W cross-section showing P-wave velocity mantle tomography observations (Mulibo and Nyblade, 2013a) that illustrate the thick Tanzanian craton underlain by hot mantle material deflected towards the eastern rift branch.

Our understanding of rift formation and evolution has matured thanks to our ability to quantify surface kinematics from geodetic data (e.g., Stamps et al., 2008; Saria et al., 2014), seismically image crustal and lithospheric structures (Whitmarsh et al., 2001; Buck, 2007; Nolet et al., 2007), and to model the mechanical behavior of a rheologically layered lithosphere in physically consistent frameworks (Burov and Poliakov, 2001; Huismans and Beaumont, 2003, 2007; Burov et al., 2007; Guillou-Frottier et al., 2012; Burov et al., 2014; Burov and

Gerya, 2014; Koptev et al., 2015). However, most continental rift models explore 2D passive rifting scenarios, probably because most of the available observational data is derived from studies of passive margins, where the records of the initial stage of rifting are buried under thick post-rift sedimentary sequences, or to fossil rifts, where the tectonic, thermal, and magmatic signatures of rifting have long decayed away. The seismically and volcanically active EARS therefore provides a unique complementary setting of a young and on-going continental rift that develops in the presence of large-scale mantle upwelling (Lithgow-Bertelloni and Silver, 1998) and slow far-field plate motions (Stamps et al., 2008; Saria et al., 2014). Here we focus on the central part of the EARS, where seismic tomography shows warm mantle material rising under the old, thick, and cold Tanzania craton (Mulibo and Nyblade, 2013a; Fig. 1). This context requires 3-dimensional thermo-mechanical models with sufficiently high resolution to accurately capture strain localization in the brittle crust, as shown in a previous, generic, study (Koptev et al., 2015). Here we follow-up on this study with a series of numerical experiments that explore various boundary conditions and initial geometrical and thermo-rheological configuration of the rift system. We test the upwelling of more than one upper mantle plume below the central EARS. Indeed, body-wave tomography shows strong indication of small-scale upper-mantle plumes rising from a single lower-mantle mega-plume ponded below the 660 km phase transition boundary (Mulibo and Nyblade, 2013a,b). We also tested the impact of plume size, temperature, composition and initial position below the Tanzanian craton, as well as the impact of the lithosphere structure and of inherited structures such as rheologically weakened suture zones along the borders of the craton.

2. Geological settings and data

The EARS is a linear active volcano-tectonic structure that cuts across the 1300 km-wide, 1100 m-high Ethiopian and East African plateaux (Fig. 1), whose high elevation is dynamically supported by whole-mantle convective upwelling (Lithgow-Bertelloni and Silver, 1998; Nyblade et al., 2000) that initiated at 30–40 Ma (Burke, 1996; Ebinger and Sleep, 1998). Passive mechanisms of EARS formation due to gravity-driven far-field forces caused by crustal thickness gradients have been also considered in earlier studies (e.g., Logatchev et al., 1972).

The lithospheric structure of the African continent is highly heterogeneous as many old suture zones of Proterozoic mobile belts were reactivated as rifts during the Paleozoic and Cretaceous (Burke, 1996). Small yet well-preserved thick cratons such as the Tanzania, Congo and Kaapvaal cratons are found throughout the EARS. These cratons, characterized by greenstone belts, tonalites, and various other high-grade metamorphic rocks, may play an important role in the localization and reactivation of deformation thanks to rheological contrasts with ancient suture zones running along their borders (e.g., McConnell, 1972; Mohr, 1982; Morley, 1988; Versfelt and Rosendahl, 1989; Ring, 1994; Corti et al., 2007; Guillou-Frottier et al., 2012).

Two eastern and western rift branches in the central EARS are superimposed onto sutures and shear zones formed by Proterozoic mobile belts that embrace the rigid Archean Tanzanian craton. Intense magmatism and continental volcanism are largely present in the eastern rift branch, while other branches such as the western rift to the west of the Tanzanian craton and the Malawi rift to the south, show only small amounts of Cenozoic volcanics. The eastern rift is characterized by a southward progression of the onset of volcanism (Baker, 1987; Ebinger, 1989; Foster et al., 1997; George et al., 1998), with widespread extension and uplift of rift

shoulders between 30 and 20 Ma (Ebinger et al., 1989; Morley et al., 1992; McDougall and Brown, 2009; Wichura et al., 2011) and the establishment of localized rift basins around 20 Ma (Ebinger, 1989; Wolfeden et al., 2004; Chorowicz, 2005; Stab et al., 2015). Using a combination of detrital zircon geochronology, tephro- and magnetostratigraphy, Roberts et al. (2012) documented the synchronous initiation and development of volcanism and basin development in the western and eastern branches of the EARS, in contrast to previous geological models that inferred a considerably younger western rift that initiated around 12 Ma only (Ebinger et al., 1989; Cohen et al., 1993; Lezzar et al., 1996; Tiercelin and Lezzar, 2002).

Most of the seismicity of the central EARS is concentrated in the narrow, amagmatic Western rift, with hypocenters reaching depths of 30–40 km and large normal faults indicative of large historical events (Yang and Chen, 2010; Moucha and Forte, 2011). In contrast, the magma-rich eastern rift is characterized by earthquake hypocenters confined to the upper ~15 km and heat flow anomalies reaching 110 mW/m² (Nyblade, 1997). These two rift branches are separated by a relatively aseismic domain centered on the 2.5–3 Ga old Tanzanian craton where seismic (Ritsema et al., 1998; Nyblade et al., 2000; Nyblade and Brazier, 2002; Weeraratne et al., 2003; Venkataraman et al., 2004; Adams et al., 2012), xenolith (Chesley et al., 1999; Lee and Rudnick, 1999), and gravity (Petit and Ebinger, 2000) data showed a 170–250 km-thick keel and a largely resisted extensional Cenozoic tectonism lithosphere that is colder and stronger than the surrounding orogenic belts. Neogene kinematics of the Nubia-Somalia plate system refers to 2 mm/yr divergence between the onset of rifting (25–30 Ma) and 4 Ma, accelerating to 4 mm/yr after 4 Ma (Stamps et al., 2008; Saria et al., 2014).

The Tanzanian craton (Fig. 1) is underlain by a broad low seismic velocity anomaly extending across the 410 km discontinuity down to the transition zone (660 km) (Nyblade et al., 2000; Huerta et al., 2009; Nyblade, 2011; Mulibo and Nyblade, 2013a,b). This anomaly is indicative of high temperature and melt presence and is consistent with the spreading of a mantle plume head beneath the craton (Weeraratne et al., 2003; Adams et al., 2012). Below the transition zone, this plume may connect with the African Superplume, a large-scale low shear-wave velocity anomaly extending from the core-mantle boundary into the mid-mantle under eastern Africa (Ritsema et al., 1999; Masters et al., 2000; Mégnin and Romanowicz, 2000; Gu et al., 2001; Grand, 2002) – though seismic data is equivocal (Ritsema et al., 2011; Simmons et al., 2011). Despite the debate on one versus two mantle plumes below the EARS based on geochemical (Rogers et al., 2000; MacDonald et al., 2001; Pik et al., 2006; Nelson et al., 2008, 2012) and geophysical (Chang and van der Lee, 2011; Hansen et al., 2012) data as well as on the results of numerical modeling (Ebinger and Sleep, 1998; Lin et al., 2005), new He, Ar, Nd, Sr and Ne isotopic data and major and trace element compositions from Neogene volcanics across the EARS suggest a common heterogeneous deep mantle source for the whole rift system (Furman et al., 2006; Furman, 2007; Chakrabarti et al., 2009; Hilton et al., 2011; Halldórsson et al., 2014), possibly indicating a source rooted in the African Superplume (Ershov and Nikishin, 2004; Bagley and Nyblade, 2013) with upward transport via localized thermal upwellings (Nyblade, 2011; Mulibo and Nyblade, 2013a,b). Here we take advantage of these recent improvements in our understanding of deep structures, geological evolution and recent kinematics together with new cutting edge numerical modeling techniques (Gerya and Yuen, 2007, see [Supplementary Methods](#)) to design a 3D ultra-high resolution viscous plastic thermo-mechanical numerical model that accounts for thermo-rheological structure of the lithosphere and hence captures the essential geophysical features of the central EARS.

3. Numerical model

3.1. 3D model setup

We use the staggered grid/particle-in-cell 3D viscous-plastic 3DELVIS code (Gerya and Yuen, 2007), based on a combination of a finite difference method applied on a staggered Eulerian grid with a marker-in-cell technique (see Supplementary Methods for more details).

3.1.1. Spatial dimensions and resolution

The spatial dimensions of the 3D model are 1500 km × 1500 km × 635 km. The regular rectangular Eulerian grid of the model domain consists of 297 × 297 × 133 nodes and offers spatial resolution of 5 km × 5 km × 5 km per grid element (Fig. 2). This implies very large mesh dimensions (more than ten million elements and hundred million randomly distributed Lagrangian markers) and hence requires unprecedented numerical efforts. The computations have taken 200 years of cumulated computing time in single CPU core equivalent (with average 4 years of single CPU core time per experiment) on SGI shared (NUMA) fat-node cluster with 2.8 Ghz Intel Xeon CPU cores.

3.1.2. Internal model structure and rheological parameters

The initial model setup comprises a stratified three-layer continental lithosphere composed of an upper and lower crust and lithospheric mantle overlaying the upper mantle. The lithosphere mantle embeds a rectangular (800 km × 400 km) cratonic block characterized by greater thickness (250 km; Smith, 1994; Ritsema et al., 1998; Mulibo and Nyblade, 2013a,b) and smaller density due to its depleted mantle composition (Connolly, 2005). The total crustal thickness is 36 km. Depth to the bottom of the embedding “normal” lithosphere is 150 km, except for the cases specified in the next section.

The mantle plume(s) was (were) initiated by seeding a temperature anomaly(ies) at the base of the upper mantle. Following Burov et al. (2007) and Koptev et al. (2015), its (their) starting geometry is modeled as a hemisphere with a radius of 200 km, except for the several test models with smaller and larger plumes (Table 1).

The initial position of the mantle plume(s) with respect to the craton is one of the parameters tested in this study (see Section 3.2).

Mantle densities, thermal expansion, adiabatic compressibility, and heat capacity are computed as function of pressure and temperature in accordance with a thermodynamic petrology model Perple_X (Connolly, 2005), which insures thermodynamically consistent variation of material properties, including phase changes. Perple_X was used in all models except for one experiment specified below. Uncertainties in mineralogical composition may result in 15–30 kg/m³ bias in thermodynamic estimates of mantle density (Watremez et al., 2013). This specifically refers to cratons, whose mantle composition may be subject to larger variations than normal lithosphere. Accordingly, we artificially decreased the craton density calculated from the standard petrology model by 15 kg/m³ to ensure initial isostatic equilibrium of the system. For the crustal rocks we used a simple Boussinesq approximation (see Supplementary Table 1) since metamorphic changes in these rocks would be of minor importance in the context of our problem.

A series of numerical experiments also explores the impact of the rheological properties of the lower crust – wet granite (WetQz) or granulite (An₇₅) – whereas the ductile part of the upper crust was represented by wet granite (WetQz) in all experiments. The latter assumption is valid since in bi-layer crusts the ductile rheology of the upper crust is of minor importance since the corresponding depth interval of 0–15 km is mainly dominated by rock-type independent brittle failure (e.g. Burov, 2011). In the models the ductile rheology of the mantle lithosphere (dry olivine) is controlled by dry olivine dislocation and Peierls creeping flow, while the sub-lithospheric mantle (dry olivine as well) deforms by diffusion creep (Caristan, 1982; Karato and Wu, 1993; Durham et al., 2009). The mantle plume is supposed to be slightly “moist” and has the rheology of wet olivine. The complete list of the rheological parameters of the model materials is provided in Supplementary Table 1.

The effectively free surface topography is implemented by inserting a 30 km thick low-viscosity “sticky air” layer between the upper interface of the model box and the surface of the crust. The viscosity of the “sticky air” is 10¹⁸ Pa s and its density is 1 kg/m³,

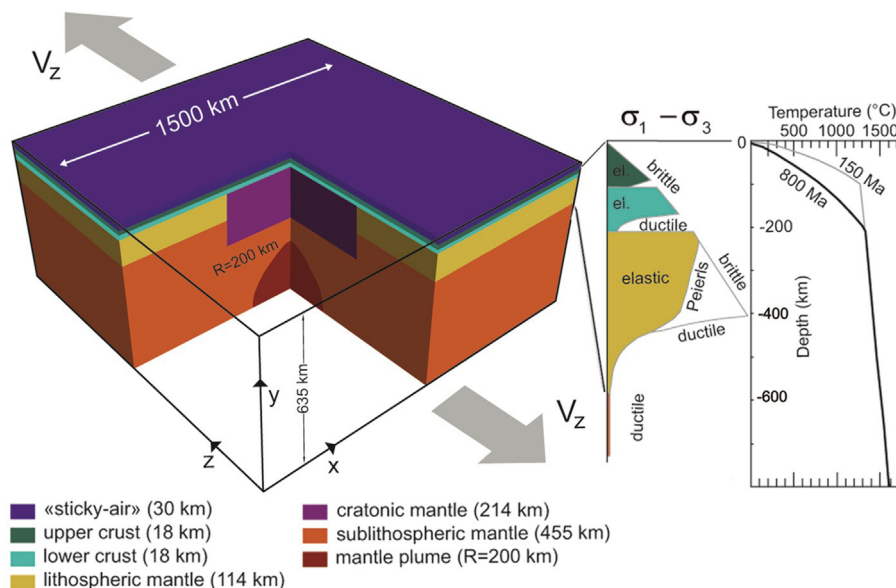


Figure 2. Model setup. Gray arrows show the velocity boundary conditions, applied in a direction perpendicular to the model domain. The initial radius of the plume is 200 km.

Table 1
Controlling parameters of the experiments.

Experiment title	Controlling parameters									
	Mantle plume(s) properties					Lithosphere properties				Boundary conditions
	Number	Initial position	Initial size (r, km)	Density	Temperature (K)	Weak rheological interface(s) craton border(s)	Rheology of lower crust	Thickness (km)		Horizontal extension velocity (mm/yr)
							Craton	"Normal" lithosphere		
1.R2	1	Center	200	Perple_X	2000	–	WetQz	250	150	3
2.R3.PosPl = North-East	1	NE (225 km) shift	200	Perple_X	2000	–	WetQz	250	150	3
3.R3.PosPl = North	1	N (200 km) shift	200	Perple_X	2000	–	WetQz	250	150	3
4.R3.PosPl = East	1	E (100 km) shift	200	Perple_X	2000	–	WetQz	250	150	3
5.R2.WeakZone = 1	1	Center	200	Perple_X	2000	One interface along west craton border	An75	250	150	3
6.R2.WeakZone = 2	1	Center	200	Perple_X	2000	Two interfaces along west and east craton borders	An75	250	150	3
7.R3.WeakZone = 1	1	NE (225 km) shift	200	Perple_X	2000	One interface along west craton border	An75	250	150	3
8.R3.WeakZone = 2	1	NE (225 km) shift	200	Perple_X	2000	Two interfaces along west and east craton borders	An75	250	150	3
9.R3.WeakZone = 3	1	NE (225 km) shift	200	Perple_X	2000	One interface along west craton border	west An75 east WetQz	250	150	3
10.R2.LongWeakZones	1	Center	200	Perple_X	2000	Two curved interfaces along west and east craton borders	An75	250	150	3
11.R3.2plume	2	NE (225 km) shift SW (225 km) shift	200 150	Perple_X	2000	–	WetQz	250	150	3
12.R3.2plume + LowCrust = An75	2	NE (225 km) shift SW (225 km) shift	200 150	Perple_X	2000	–	An75	250	150	3
13.R3.2plume + BigPlume	2	NE (225 km) shift SW (225 km) shift	200 175	Perple_X	2000	–	An75	250	150	3
14.R3.2plume + HotPlume	2	NE (225 km) shift SW (225 km) shift	200 150	Perple_X	2000 2100	–	An75	250	150	3
15.R3.2plume + LightPlume	2	NE (225 km) shift SW (225 km) shift	200 150	Perple_X	2000	–	An75	250	150	3
16.R3.2plume.EqualSize	2	NE (225 km) shift SW (225 km) shift	200 150	Perple_X Perple_X -30 kg/m ³	2000	–	WetQz	250	150	3
17.R3.2plume + WeakZone = 2	2	NE (225 km) shift SW (225 km) shift	200 150	Perple_X	2000	Two interfaces along west and east craton borders	An75	250	150	3
18.R3.E = 50; N = 100	1	NE (112 km) shift	250	Perple_X	2000	–	WetQz	250	150	3
19.R3.E = 5; N = 10	1	NE (11 km) shift	250	Perple_X	2000	–	WetQz	250	150	3
20.R3.E = 10; N = ~20–30	1	NE (~25 km) shift	250	Perple_X	2000	–	WetQz	250	150	3
21.R3.E = 10; N = ~20–30 + R = 200	1	NE (~25 km) shift	200	Perple_X	2000	–	WetQz	250	150	3
22.R3.E = 10; N = ~20–30 + WeakZone = 2	1	NE (~25 km) shift	250	Perple_X	2000	Two interfaces along west and east craton borders	An75	250	150	3
23.R2.H_lit = 150–200	1	Center	200	Perple_X	2000	–	WetQz	250	west 200 east 150	3
24.R3.H_lit = 150–200 + W = ~25-50	1	W (~25–50 km) shift	200	Perple_X	2000	–	WetQz	250	west 200 east 150	3
25.R3.H_lit = 150–200 + W = 75	1	W (75 km) shift	200	Perple_X	2000	–	WetQz	250	east 150 west 200	3

(continued on next page)

Table 1 (continued)

Experiment title	Controlling parameters				Lithosphere properties				Boundary conditions	
	Mantle plume(s) properties				Temperature (K)	Weak rheological interface(s) craton border(s)	Rheology of lower crust	Thickness (km) Craton	"Normal" lithosphere	Horizontal extension velocity (mm/yr)
	Number	Initial position	Initial size (r, km)	Density						
26.R3.H_lit = 150–200 + W = 100	1	W (100 km) shift	200	Perple_X	2000	–	WetQz	250	east 150 west 200	3
27.R3.H_lit = 150–200 + W = 50 + BigPlume	1	W (50 km) shift	400–200	Perple_X	2000	–	WetQz	250	east 150 west 200	3
28.R3.R = 150 + LC = WetQz	1	NE (225 km) shift	150	Perple_X	2000	–	WetQz	250	150	3
29.R3.R = 150 + LC = An75	1	NE (225 km) shift	150	Perple_X	2000	–	An75	250	150	3
30.R3.R = 200 + LC = An75	1	NE (225 km) shift	200	Perple_X	2000	–	An75	250	150	3
31.R3.R = 300 + LC = An75	1	NE (225 km) shift	300	Perple_X	2000	–	An75	250	150	3
32.R3.H_crat = 200	1	NE (225 km) shift	200	Perple_X	2000	–	WetQz	200	150	3
33.R3.Vext = 1.5	1	NE (225 km) shift	200	Perple_X	2000	–	WetQz	250	150	1.5
34.R3.LC = An75 + Vext = 6	1	NE (225 km) shift	200	Perple_X	2000	–	An75	250	150	6

according to optimal parameters established in the previous studies (Duretz et al., 2011; Cramer et al., 2012; Burov and Gerya, 2014).

3.1.3. Velocity boundary conditions

Although some have proposed dominant deviatoric compression acting on the African plate in consideration of surrounding mid-ocean ridges (e.g., Zeyen et al., 1997), calculations of deviatoric stresses arising from lateral gradient of gravitational potential energy (GPE) due to elevation – most of eastern and southern Africa being at elevations > 1500 m – and lateral density variations show that the EARS undergoes ~10 MPa of E–W extensional deviatoric stresses (Coblentz and Sandiford, 1994; Stamps et al., 2010, 2014). This is equivalent to a force per unit length of 1 TN/m for a 100 km-thick lithosphere, of the same order as slab pull forces. This extensional deviatoric stress regime is the source of the far-field extension, which, in our models, is applied as a kinematic boundary condition.

We simulate this weak tectonic forcing by applying a constant divergent velocity normal to the “eastern” and “western” sides of the model box. Following geological and geodetic estimates for the EARS extension rates, we varied this velocity between 1.5 and 6 mm/yr (Table 1). The corresponding horizontal forces on the borders of the model are small (on the order of typical ridge push forces, i.e. $(1–2) \times 10^{11}$ N per unit length). Free slip boundary conditions are used on the “northern” and “southern” sides of the model, which are not subject to extension. Compensating vertical influx velocities through the upper and lower boundaries are introduced to ensure mass conservation in the model domain (Gerya, 2010).

3.1.4. Initial temperature distribution and thermal boundary condition

The initial geotherm is one of the variable parameters of our experiments. In the reference experiment, the initial geotherm is piece-wise linear, with 0 °C at the surface (≤ 30 km, the air), 400 °C at the upper/lower crustal interface, 700 °C at the Moho, 1300 °C at the bottom of the lithosphere (i.e. deeper below the craton and shallower below the embedding lithosphere) and 1630 °C at the bottom of the model domain at 635 km depth. The resulting adiabatic thermal gradient in the mantle is 0.5–0.7 °C/km. The mantle plume(s) has (have) an initial temperature of 2000 °C (except for one model, see Section 3.2). We chose an initial mantle plume temperature of 2000 °C, 300 °C warmer than the surroundings, consistent with the 20–40 km depression of the 410 km discontinuity observed seismically beneath the Tanzanian craton (Huerta et al., 2009).

The thermal boundary conditions correspond to fixed temperature values at the upper surface and the bottom of the model (0 and 1630 °C, respectively; Koptev et al., 2015) and zero horizontal heat flux across the vertical boundaries.

3.2. Experiments and key variable parameters

We tested 34 different experimental settings by varying ten controlling parameters that characterize the properties of plume(s) and lithosphere and the velocity boundary conditions (Table 1):

- (1) Number of mantle plumes;
- (2) Initial position of the mantle plume(s) with respect to the craton;
- (3) Initial size of the mantle plume(s);
- (4) Density of the mantle plume(s);
- (5) Temperature of the mantle plume(s);
- (6) Presence, number and shape of the weak rheological interface(s) along the craton border(s);

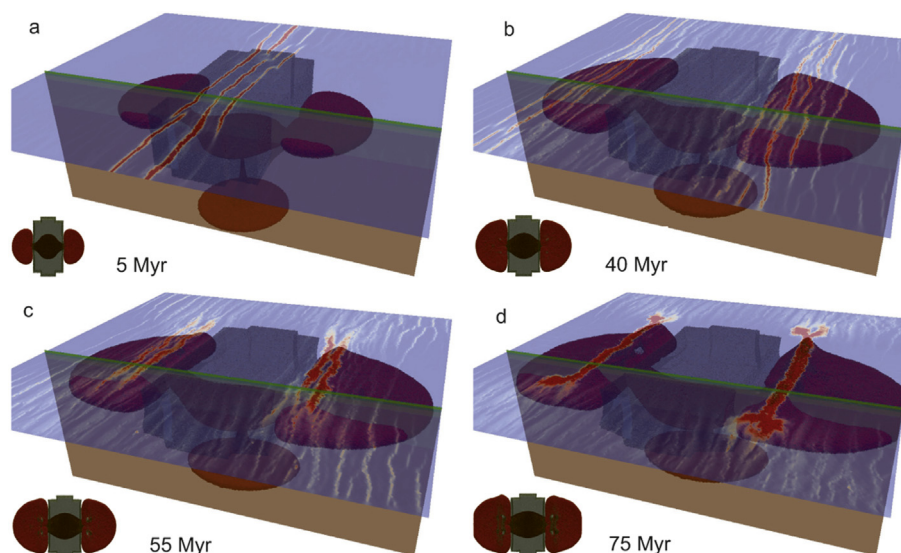


Figure 3. Reference model (Model **1**, Table 1). Craton is the dark gray quasi-rectangular volume. The plume material is shown in dark red. Blue to red colors at the model surface indicate cumulative strain due to faulting.

- (7) Rheology of the lower crust;
- (8) Craton thickness;
- (9) Normal (non-cratonic) lithosphere thickness;
- (10) Horizontal extension velocity.

We started our experiments with a reference model (Fig. 3, model **1.R2**) characterized by a single mantle plume (initial hemisphere radius of 200 km, initial temperature of 2000 °C, and dynamic P-T dependent density structure defined by the thermodynamic model *Perple_X*, Connolly, 2005). In this reference experiment the initial plume is seeded exactly below the central part of the craton and the lithosphere does not contain any weak predefined rheological zones; the rheology of its lower crust refers to wet quartzite (*WetQz*). The thicknesses of the “normal” and “cratonic” lithosphere correspond to commonly inferred values of 150 and 250 km, respectively (e.g., Burov et al., 2007; Guillou-Frottier et al., 2012). The horizontal velocities applied along the “eastern” and “western” sides of the model are 3 mm/yr.

The first parameter that has been varied in the experiments is the initial position of the plume with respect to the center of the craton. The models **2.R3.PosPL** = North-East, **3.R3.PosPL** = North and **4.R3.PosPL** = East correspond to a lateral shift of the mantle plume to the NE (225 km), to the north (200 km) and to the east (100 km), respectively. Note that all of the models listed below refer to either central plume position (prefix R2) or to that characterized by a north-east shift (prefix R3), except for the models with a different thicknesses of the “normal” lithosphere (models **28–31**), where the initial plume position has been shifted westward (see below).

The next series of experiments (models **5–10**) is characterized by a weak narrow vertical interface(s) between the craton and the embedding lithosphere that mimics suture zones. These zones have rheological parameters of the upper crust: for the “weak” zone(s) along long the side(s) of the craton we used granite (*WetQz*) rheology whereas the surrounding area of the lower crust consists of mafic (*An75*) rocks. Therefore the implemented weak zones are not over-softened and are weaker than the surroundings within the depths below the upper-lower crustal interface. Several models with one and two weak interfaces (in presence of centered and NE shifted plume) have been implemented (models

5.R2.WeakZone = 1, **6.R2.WeakZone** = 2, **7.R3.WeakZone** = 1 and **8.R3.WeakZone** = 2). Also we have tested the configurations with one weak zone welded into stronger crust within the western part of model and weak lower crust for the entire opposite half of the studied domain (model **9.R3.WeakZone** = 3). Finally, the curved shape of two weak interfaces embracing cratonic bloc has been tested in the model **10.R2.LongWeakZone**.

The experiments with two plumes (models **11–17**) containing a second mantle plume shifted to the southwest (225 km) from the center of the craton. The first two experiments of this series (**11.R3.2plume** and **12.R3.2plume** + *LowCrust* = *An75*) refer to different rheologies of the lower crust (*WetQz* and *An75*, respectively) whereas the second plume has the same parameters as the first one, except for a slightly smaller radius of 150 km. The next 3 models were implemented with the goal to explore the sensitivity of the model **12** to the properties of the second plume. In these experiments the second plume has been made, respectively, bigger (initial radius of 175 km, model **13.R3.2plume** + *BigPlume*), hotter (initial temperature of 2100 °C, **14.R3.2plume** + *HotPlume*), and lighter (*Perple_X*-derived density was artificially reduced by 30 kg/m³, **15.R3.2plume** + *LightPlume*). Two plumes of the same size (200 km) were tested in model **16.R3.2plume.EqualSize** whereas model **17.R3.2plume** + *WeakZone* = 2 refers to the additional introduction of two weak interfaces along the craton borders into the setup of the model **11**.

The impact of much smaller initial NE shifts and of slightly bigger ($r = 250$ km) initial plume are studied in experiments **18.R3.E** = 50; $N = 100$ (shift is 112 km; eastward component is 50 km, northward component is 100 km), **19.R3.E** = 5; $N = 10$ (shift is 11 km; eastward component is 5 km, northward component is 10 km) and **20.R3.E** = 10; $N = \sim 20–30$ (shift is ~ 25 km; eastward component is 10 km, northward component is 20–30 km). Model **21.R3.E** = 10; $N = \sim 20–30$ + $R = 200$ refers to a shift of ~ 25 km for the reference plume size ($r = 200$ km). Inserting two weak zones into the model **20** yields model **22.R3.E** = 10; $N = \sim 20–30$ + *WeakZone* = 2.

The series of experiments with different thicknesses of “normal” lithosphere (150 km within eastern half of model domain, 200 km within western one) starts with a central initial position of a plume of reference size ($r = 200$ km) (model **23.R2.H_lit** = 150–200). Then

we sequentially shift the mantle plume to ~ 25 – 50 , 75 and 100 km westward (models **24.R3.H_lit** = 150 – 200 + W = ~ 25 – 50 , **25.R3.H_lit** = 150 – 200 + W = 75 and **26.R3.H_lit** = 150 – 200 + W = 100 , respectively). We combine a model with a hemispherical plume shifted by 50 -km has with a hemi-ellipsoidal plume of bigger size (horizontal radius of 400 km; vertical radius of 200 km) to design model **27.R3.H_lit** = 150 – 200 + W = 50 + BigPlume.

Models **28**–**31** refer to different sizes (r = 150 , 200 and 300 km) of the north-east shifted (225 km) plume in presence of different lower crustal rheologies (WetQz or An₇₅).

Finally, the last 3 models (models **32**–**34**) illustrate the impact of craton thickness (model **32.R3.H_crat** = 200) and velocity boundary conditions (the models with slower (**33.R3.Vext** = 1.5) and faster (**34.R3.LC** = An₇₅ + Vext = 6) external extension).

Every model run took about 4 years of CPU time (2 month of physical run time on a shared memory SGI parallel supercomputer).

4. Experimental results

4.1. Reference model (Model 1)

The reference model **1.R2** shows a rapid plume ascent after the experiment onset: the mantle plume reaches the bottom of the cratonic lithosphere in 0.5 Myr, which is similar to previous models with cratons (Burov et al., 2007; Koptev et al., 2015). The cratonic block causes the plume head to split into two initially nearly symmetrical parts, each of which flows towards the base (LAB) of the “normal” lithosphere near the craton borders (Fig. 3a). As shown in Koptev et al. (2015), brittle strain localization in the crust, initially caused by far-field stresses, is amplified by heat transport and serves to channelize the plume material, without requiring regions of pre-existing thinning or rheological weakness. This channeling helps localizing strain in two symmetric narrow north-

south rifts above the zones of plume heads emplacement (Fig. 3b). This positive feedback between lithospheric thinning and channelized flow of the plume material is a key mechanism for strain localization in the models.

The next stage of the system development corresponds to localized ascent of the plume material (at 55 Myr) along the narrow and stretched zones (Fig. 3c) that further leads to fast (<1 Myr) destruction of the continental crust (at 75 Myr, Fig. 3d) by hot mantle material and transition from pre-breakup rifting to post-breakup spreading (>75 Myr).

Strain distribution within the crust shows two symmetric N–S stretched (i.e. perpendicular to far-field extension) rifting zones appearing simultaneously on either side of craton just above mantle hot material concentrated below the lithosphere-aesthenosphere boundary (Fig. 3).

4.2. Initial position of the mantle plume with respect to the craton (Models 2–4)

The initial position of the mantle plume with respect to the craton is one of the most important parameters tested in this study (Table 1). Fig. 4 shows that different initial plume positions (models 2–4) result in very different evolutions of the system compared to the reference model (model 1). A common feature of these models is the deflection of plume material by the craton and the formation of a local uplift centered above a secondary plume head. The direction of this deviation of the plume material by the cratonic block is controlled by the initial position of the plume, whereas strain localization within the upper crust (horizontal slices on the Fig. 4) is conditioned by the spatial distribution of hot material ponding under “normal” lithosphere. The model with a plume head deflected to the north (**3.R3.PosPl** = North, Fig. 4b) shows strain localization within the central part of the model domain, while models with a east and north-east shifted plume (**4.R3.PosPl** = East

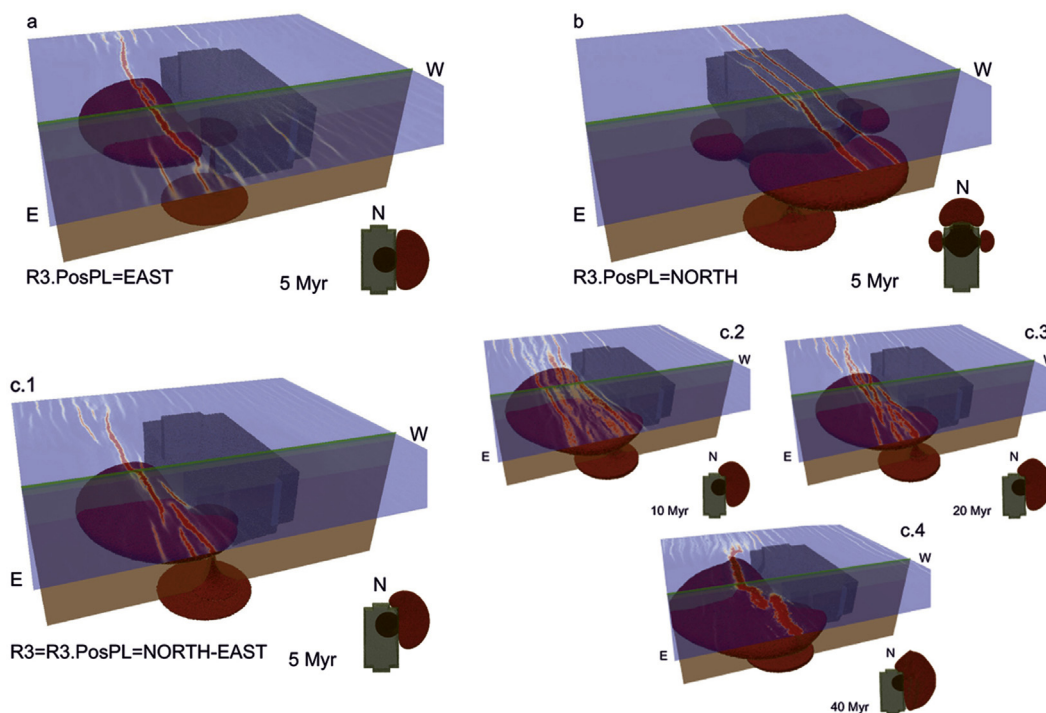


Figure 4. Models with different initial position of mantle plume with respect to craton (Models 2–4, Table 1).

(Fig. 4a) and 2.R3.PosPl = Northeast (Fig. 4c)) both show an eastward displaced rift.

The central cratonic block, less deformable than the surrounding lithosphere, moves eastward and rotates slowly anticlockwise (model 2.R3.PosPl = Northeast, Fig. 4c). This rotation is consistent with observed geodetic displacements (Stamps et al., 2008; Saria et al., 2014). It results from the torque due to asymmetrically distributed forces exerted by the plume material on the craton keel. The deflection of the plume material towards the eastern rift basins, together with the lateral motion of the cratonic block driven by the plume, preserves the craton from thermo-mechanical erosion until the system reaches steady state at 20 Myr (Sleep et al., 2002). This provides new insights for understanding of the survival of small cratonic terrains.

As shown above, models 2 and 4 (Fig. 4a,c) are in good agreement with the observations in the EARS, as they reproduce the magmatic eastern branch and of the anticlockwise rotation of the craton. However, these models do not reproduce the observed strain localization along the western margin of the cratonic bloc in the western rift branch.

4.3. Rheological properties along the craton borders (Models 5–10)

The most obvious way to produce strain localization is to locally impose weaker rheological properties (e.g. McConnell, 1972; Mohr, 1982; Ring, 1994; Corti et al., 2007; Guillou-Frottier et al., 2012). Thus, to allow for rift formation along the western side of the craton, we perform model 7.R3.WeakZone = 1 (Supplementary Fig. 1c), a variation of model 2 (Fig. 4c) where we insert of zone of weaker (WetQz) rheology between the western side of the craton and the embedding lithosphere. To test more symmetrical and geologically consistent cases we also conducted experiment 8.R3.WeakZone = 2 (Supplementary Fig. 1d) with two weak interfaces along both sides of the craton.

The results of these models expectedly show additional zones of deformation along the western boundary of craton (Supplementary Fig. 1c,d). The only difference between these two models is the more restricted fault distribution within the “magmatic” rift branch in model 8 (Supplementary Fig. 1d), due to the predefined eastern weak zone.

To make the style of deformation within the eastern branch more similar to that of model 2, we designed model 9.R3.WeakZone = 3 (Supplementary Fig. 1e) with only one western weak interface (as in model 7, Supplementary Fig. 1c) and a weaker rheology of the lower crust for the entire eastern part of the model domain (note that the lower crustal rheology of the model 2 (Fig. 4c) is that of wet quartzite (weak) everywhere). This model shows the same timing and style of deformation on the eastern “hot” side of the craton as in model 2, but also shows the formation on an additional zone of deformation along the opposite craton boundary, a feature in better agreement with geological observations within the EARS (Supplementary Fig. 1e).

Supplementary Fig. 1f shows the results of model 10.R2.Long-WeakZones characterized by a central plume position and a more complex geometry of weak zones. It aims at reproducing more accurately the embracing shape of the EARS rift branches around the Tanzanian craton.

Models with a central plume position in the presence of weak zones (models 5.R2.WeakZone = 1 and 6.R2.WeakZone = 2) are shown in Supplementary Fig. 1a,b.

Note that model 5 that contains only one weak interface (along the western edge of the craton, Supplementary Fig. 1a) demonstrates the asymmetry not only at the crustal level as deformation expectedly develops only within this predefined weak zone, but also in the deep mantle plume where the plume ascent takes place

only within its westward deflected half. This indicates that the rheological properties of the continental crust not only impact the surface morphology and crustal strain patterns, but also influence the distribution of plume head material at depth, which, in turns, bears consequences for magmatic processes and mantle lithosphere stability.

4.4. Two-plumes (Models 11–17)

Recent seismic tomography data indicates the presence of a second, possibly smaller, mantle plume under the western branch of the EARS (Mulibo and Nyblade, 2013a,b). Such secondary upper mantle plumes could be stemming from the ponding of superplume material beneath the 660 km discontinuity (Yuen et al., 2007).

We tested this hypothesis with a series of experiments containing two mantle plumes. The first one is shifted to the NE as in most of previous models, the second one is smaller ($r = 150$ km versus $r = 200$ km for the “ordinary” first plume) and shifted to the SW.

The first model in this series (model 11.R3.2plume, Fig. 5) shows that the upwelling of a bigger plume starts much faster (Fig. 5a,b), which causes the initiation of the eastern branch in the absence of visible deformation at the opposite side of the craton. After 15 Myr the head of the second plume, deflected by the craton, reaches the bottom of “normal” lithosphere (Fig. 5c) to the west where it causes strain localization less pronounced than in the east (Fig. 5d).

These results are weakly sensitive to variations of lower crust rheology (Supplementary Fig. 2a) and properties of the second mantle plume (size (Supplementary Fig. 2b), initial temperature (Supplementary Fig. 2c) and density (Supplementary Fig. 2d)). Models 12–15 show mostly differences in timing and initiation of the western branch (Supplementary Fig. 2).

Model 16.R3.2plume.EqualSize (Supplementary Fig. 3) with mantle plumes of equal size ($r = 200$ km) show simultaneous and symmetric upwelling and deflection causing pure anti-clockwise rotation of craton block in contrast of all previous “asymmetric” models where anti-clockwise rotation of the craton is combined with its westward motion. Note that the position of the craton in reference model 1, on the contrary, remains stationary over the 80 Myrs of the model (Fig. 3).

Model 17.R3.2plume + WeakZone = 2 that combines an additional small plume shifted to the SE and weak interfaces along the craton borders, does not show much difference with the other models in this series, except for more localized strain distribution in the rifts as expected given the narrow predefined weak zones (Supplementary Fig. 4).

4.5. Small NE shifts of the initial position of the mantle plume (Models 18–22)

This series of experiments shows that the asymmetrical distribution of hot mantle material on the both sides of the craton causing EARS-like rifting with two coeval asymmetric branches can be reproduced not only under the assumption of two mantle plumes of different size shifted in opposite directions, but also by adjusting the initial position of a slightly scaled-up ($r = 250$ km) single plume.

Model 18.R3.E = 50; N = 100 (Fig. 6a) is characterized by an initial NE shift of the plume that is twice smaller than in previous models (112 km instead of 225 km). However, it still shows full deflection of the plume material toward one side of the craton as it is observed in above-mentioned models with initially “shifted” plumes. On the contrary, a small (only 11 km) shift of the plume position to the NE (model 19.R3.E = 5; N = 10) results in an almost symmetrical plume head splitting in both directions and quasi-

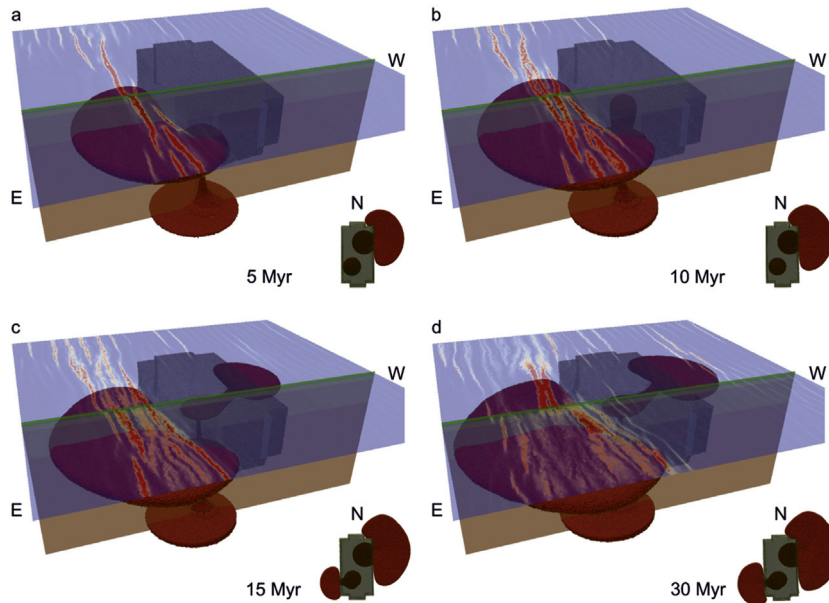


Figure 5. Model with 2 mantle plumes (Model 11, Table 1).

symmetrical crustal strain distribution similar to reference model 1 (Fig. 6b). However, increasing the initial shift to ~ 25 km (model 20.R3.E = 10; N = ~ 20 –30) leads to plume head separation into two non-equal parts, which results in a distribution of mantle plume material and crustal deformation roughly similar to models with two plumes (Fig. 6c).

Model 20 shows large amounts of melt produced on the rifted eastern side of the craton whereas the western border remains less deformed and relatively magma-poor. Melt is produced as a result of both adiabatic decompression as the plume rises, and of the extra heat advected by the plume itself, leading to generation of both,

plume-derived and mantle-lithosphere-derived melts (Fig. 7). The mixing of plume-derived and lithospheric mantle-derived melts is consistent with geochemical data from Kenyan rift volcanics (Spath et al., 2001). This melting, in turn, increases the rate of lithospheric thinning under the eastern rift branch.

Model 21.R3.E = 10; N = ~ 20 –30 + R = 200 illustrates the important role of the plume size in asymmetric plume head separation: a “standard-size” plume ($r = 200$ km) does not provide enough material for splitting in both directions, which leads to single-side deflection of the plume head as in the “long-shifted” models (Supplementary Fig. 5).

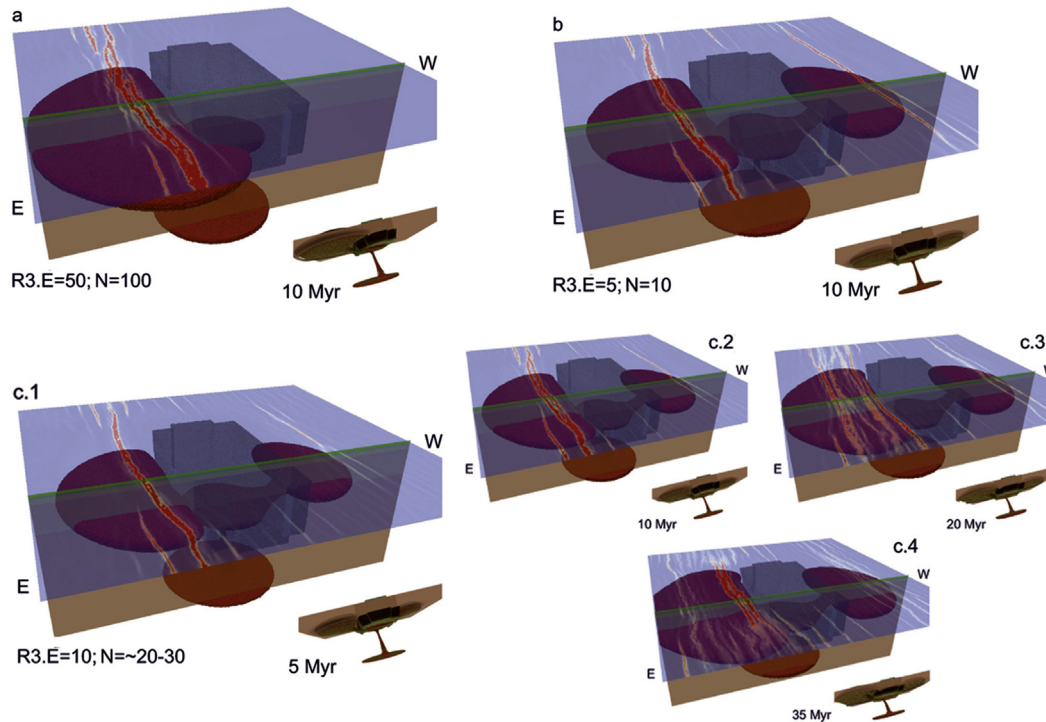


Figure 6. Models with small NE shifts of initial position of bigger ($r = 250$ km) mantle plume (Models 18–20, Table 1).

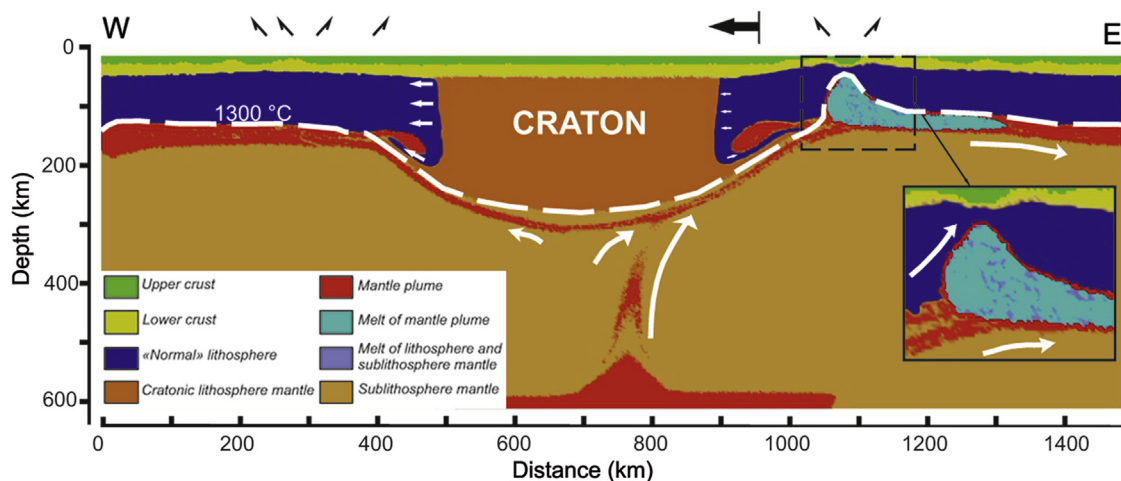


Figure 7. Distribution of plume material and melt in the model **20** (Table 1), EW model cross-section at 45 Ma that best-fits observations in the EARS, shows plume head separation onto two non-equal parts. The 1300 °C isotherm delineates the base of the lithosphere. The plume splitting and deflection preserves the craton keel while the deflected material thermally erodes the mantle lithosphere to the east of the craton and pushes the craton to the west. The produced melt percolates within the partially molten region and accumulates below the rift axis. It combines plume-derived and mantle-lithosphere components and has a strong effect on the upwelling velocity within asthenospheric wedge below the axis of the “eastern” rift (right). Black arrow indicates initial position of craton border.

The addition of two weak zones along the craton borders to the most “successful” model of this series (model **20**) does not significantly modify the results (model **22.R3.E** = 10; $N = \sim 20\text{--}30 + \text{WeakZone} = 2$; Supplementary Fig. 6).

4.6. Thicknesses of the embedding lithosphere (Models **23–27**)

There is geological and geophysical evidence that the thickness of the lithosphere embedding the Tanzanian craton is larger to the west than to the east (Artemieva and Mooney, 2001; Artemieva, 2006). We conducted experiments (models **23–27**) with an embedding lithosphere considerably thicker in the western half of the model domain (200 km) than in the eastern one (150 km) while keeping a 250 km-thick craton.

The most interesting feature of this model series is that a central initial plume position (**23.R2.H_lit** = 150–200, Fig. 8) and even a slightly (25 km and 50 km; Supplementary Fig. 7a,e) west-shifted plume (**24.R3.H_lit** = 150–200 + E = $\sim 25\text{--}50$) lead to the complete deflection of the plume head to the east as in model **4**). Models with a larger initial plume show similar results (**27.R3.H_lit** = 150–200 + W = 50 + BigPlume, Supplementary Fig. 7b,f). Only models with a westward shift of the plume position by 100 km (model **26.R3.H_lit** = 150–200 + W = 100) provides the deviation of the bulk of the plume material to the western side of the craton (Supplementary Fig. 7c,g). An initial shift of 75 km (the model **25.R3.H_lit** = 150–200 + W = 75; Supplementary Fig. 7d,h) leads to plume head separation into two non-equal parts as in model **20.R3.E** = 10; $N = \sim 20\text{--}30$ (Fig. 6c).

The magmatic eastern branch of the EARS is associated with thinner lithosphere (150 km; Artemieva and Mooney, 2001; Artemieva, 2006) while the magma-poor western rift branch develops in a much thicker one (200 km). In case of equal thickness of “normal” lithosphere this contrasted distribution of the magmatic activity can be explained by a significant eastward shift of the uprising plume with respect to the craton, which results in the eastward deflection of the plume head by the cratonic keel (e.g., models **2** and **4**).

However, models with different (in western and eastern segments) thicknesses of the embedding “normal” lithosphere show that only considerable westward shift of the initial plume position (about 75–100 km, i.e. $\frac{1}{4}$ of craton width) (models **25–26**) result in large-scale magmatism to the west of the craton whereas central

(models **23–24**, **27**) and, obviously, eastward-shifted initial plume position result in deviation of the uprising hot material to the east.

4.7. Plume size (Models **28–31**)

We performed models with significant (225 km) NE shifts in the initial plume position to explore the impact of the plume size ($r = 150, 200$ and 300 km, models **28–31**). In general, these models show a similar evolution of strain within the upper crust (Supplementary Fig. 8). Only the combination of a small plume ($r = 150$ km) with weak (WetQz) lower crust rheology (model **28.R3.R** = 150 + LC = WetQz) leads to considerable differences in timing of the rifting processes (Supplementary Fig. 8a).

These results, however, do not permit to conclude that the plume-head size has no effective impact on system evolution since the above mentioned experiments with smaller initial shift (models **18–22**) demonstrate different modes of system development (from asymmetric splitting (model **20**) to full deflection of plume head (model **21**)) resulting from to plume-head size variation.

4.8. Additional experiments (Models **32–34**)

Model **32.R3.H_crat** = 200 with a thinner (200 km) craton show different strain distribution within the upper crust compared to all previous models (Supplementary Fig. 9c). Varying the boundary velocities (models **33.R3.Vext** = 1.5 and **34.LC** = An₇₅ + Vext = 6) only affects the timing of the main events (onset of rifting, beginning of the plume ascent, continental crust break-up, and transition to spreading) without significant impact on the other model output features (Supplementary Fig. 9a,b).

5. Discussion and conclusions

Our experiments show that a complex double rift system can develop from relatively simple initial conditions. In our particular scenario the system, submitted to weak far-field tensional stress, evolves as a consequence of the deflection of a rising mantle plume by a craton keel. This particular model produces features that bear strong similarities with first-order geological and geophysical observations in the EARS. Overall, our results reconcile the active (plume-activated) and passive (far-field tectonic stresses) rift

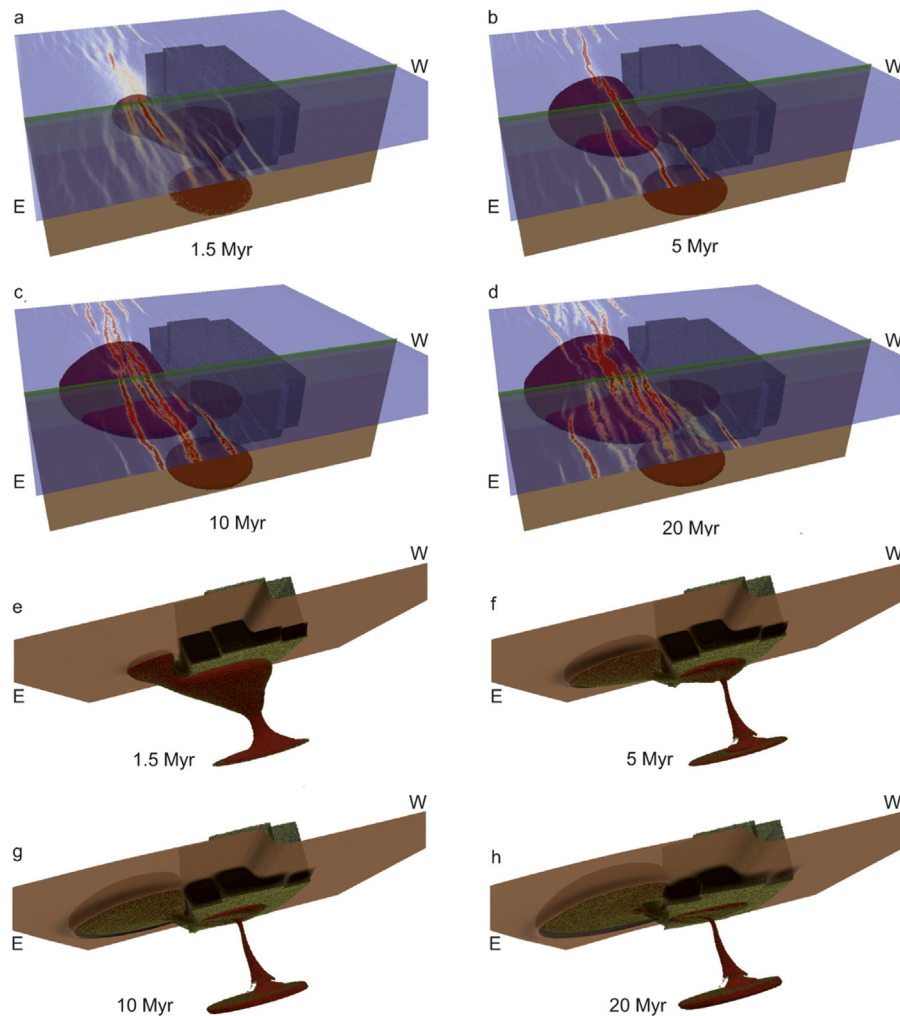


Figure 8. Model with different thicknesses (150 km within eastern half of the model domain and 200 km within western one) of the embedding “normal” lithosphere (Model 23, Table 1). Brown surface on Fig. 8e,f,g,h corresponds to the lithospheric bottom.

concepts demonstrating that both magmatic and a-magmatic rifts may develop in identical geotectonic environments.

A feature common to all experiments is the rapid ascent of a mantle plume toward the bottom of the craton, followed by the deflection and/or splitting of the plume head, depending on the initial position of the plume. This results in the ponding and lateral spreading of the plume material at the base of the thinner lithosphere that embeds the craton, as also observed in previous 2D experiments (Burov and Guillou-Frottier, 2005; Burov et al., 2007; Burov and Cloetingh, 2010; Guillou-Frottier et al., 2012). The initial position of the strain localization zones – the future rift basins – within the upper crust is controlled by the presence of weak zones in the crust and by the distribution of plume material ponding below the lithosphere that surrounds the craton.

A small asymmetry in the initial position of the plume can lead to a strongly asymmetric system evolution. A rift zone forms along the eastern side of the craton with significant melt production from mantle plume material (Baker, 1987; Ebinger et al., 1989), analogous to the eastern magmatic branch of the EARS. To explain the formation of an asymmetric system with the coeval initiation of the amagmatic western branch and magmatic eastern branch as observed in the central EARS, we experimentally explored several scenarios of which three can be retained as specifically pertaining to the EARS (Fig. 9):

- (1) The most trivial scenario assumes mechanically weak vertical interfaces simulating the suture zone observed in the geology along the western border of the craton only (model 7). In this case the initial position and the size of the plume are relatively unimportant.
- (2) A second scenario involves a second smaller plume initially shifted to the SW (model 11). In this case, rift basins develop on both sides of the craton with no need for weakening the interface between the craton and the embedding lithosphere.
- (3) Finally, a broad mantle plume whose initial position is slightly shifted to the eastern side of the craton also results in contrasted double-rifting with an asymmetric distribution of mantle material on either side of the craton (model 20). This model does not require weakening the interface between the craton and the embedding lithosphere.

It is not possible at this point to choose a preferred scenario because adequate data in the central EARS are still quite sparse. However, it is noteworthy that only the third scenario is compatible with two important features of the geological evolution of the EARS, (1) the quasi-simultaneous initiation of both rift branches (Roberts et al., 2012) and (2) their feeding from a single mantle source according to geochemistry data (Chakrabarti et al., 2009; Hilton et al., 2011; Halldórsson et al., 2014). Under this scenario,

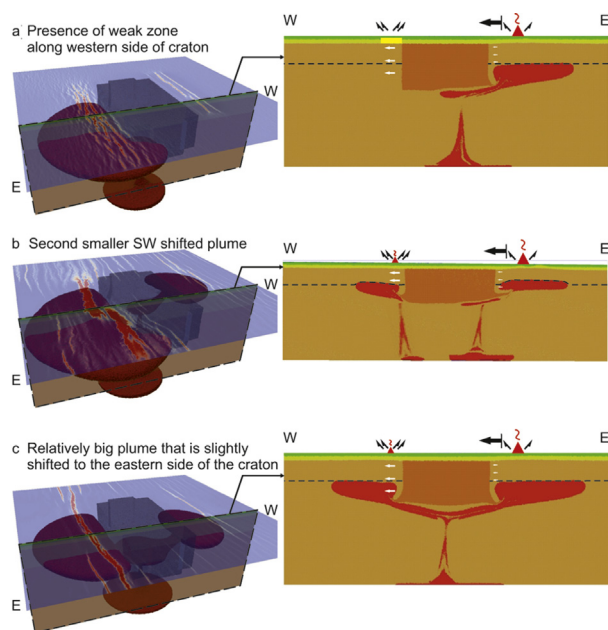


Figure 9. Three possible scenarios explaining main EARS features. (a) The assumption of rheologically weak interface along the western border of the craton (Model 7); (b) the presence of second smaller plume initially shifted in SW direction (Model 11); (c) the unequal splitting of relatively big plume which initial position is slightly shifted to the eastern side of the craton (Model 20).

models with a thicker lithosphere to the west of the craton, as indicated by geophysical observations (Artemieva and Mooney, 2001; Artemieva, 2006) that provided the best fit to observations by further increasing rift asymmetry and favoring intense magmatism along the eastern border of the Tanzania craton.

Acknowledgements

We thank an anonymous reviewer for comments that helped improved this paper. This study is co-funded by a U.S. National Science Foundation (Grant EAR-0538119) to E. Calais, by the Advanced ERC (Grant 290864 RHEOLITH) to E. Burov and A. Koptev and by the Royal Academy of Netherlands visiting professor grant to E. Burov, by BRGM to E. Burov and L. Guillou-Frottier and by the UPMC visiting professor grant to S. Cloetingh. The numerical simulations were performed on the ERC-funded SGI Ulysse cluster of ISTEP.

Appendix A. Supplementary data

Supplementary data related to this article can be found at <http://dx.doi.org/10.1016/j.gsf.2015.11.002>.

References

Adams, A., Nyblade, A., Weeraratne, D., 2012. Upper mantle shear wave velocity structure beneath the East African plateau: evidence for a deep, plateau-wide low velocity anomaly. *Geophysical Journal International* 189, 123–142.

Armitage, J.J., Ferguson, D.J., Goes, S., Hammond, J.O.S., Calais, E., Rychert, C.A., Harmon, N., 2015. Upper mantle temperature and the onset of extension and break-up in Afar, Africa. *Earth and Planetary Science Letters* 418 (0), 78–90.

Artemieva, I.M., 2006. Global $1^\circ \times 1^\circ$ thermal model TC1 for the continental lithosphere: Implications for lithosphere secular evolution. *Tectonophysics* 416, 245–277.

Artemieva, I.M., Mooney, W.D., 2001. Thermal thickness and evolution of precambrian Lithosphere: a global study. *Journal of Geophysical Research: Solid Earth* 106 (B8), 16387–16414.

Bagley, B., Nyblade, A.A., 2013. Seismic anisotropy in eastern Africa, mantle flow, and the African superplume. *Geophysical Research Letters* 40, 1500–1505.

Baker, B.H., 1987. Outline of the petrology of the Kenya rift alkaline province. In: Fitton, J.G., Upton, B.G.J. (Eds.), *Alkaline Igneous Rocks*, Geological Society [London] Special Publication, 30, pp. 293–311.

Behn, M.D., Buck, W.R., Sacks, I.S., 2006. Topographic controls on dike injection in volcanic rift zones. *Earth and Planetary Science Letters* 246, 188–196.

Buck, W.R., 2007. In: Watts, A.B. (Ed.), *The Treatise on Geophysics*, 6. Elsevier.

Buck, W.R., 1991. Modes of continental extension. *Journal of Geophysical Research* 96, 20161–20178.

Buck, W.R., 2006. The role of magma in the development of the Afro-Arabian Rift System. In: Yirgu, G., Ebinger, C.J., Maguire, P.K.H. (Eds.), *The Afar Volcanic Province within the East African Rift System*, Geological Society, London, Special Publications, 259, pp. 43–54.

Burke, K., 1996. The African plate. *South African Journal of Geology* 99, 339–409.

Burov, E., 2011. Rheology and strength of the lithosphere. *Marine and Petroleum Geology* 28 (8), 1402–1443.

Burov, E., Cloetingh, S., 2010. Plume-like upper mantle instabilities drive subduction initiation. *Geophysical Research Letters* 37 (3), 202–217.

Burov, E., Francois, T., Yamato, P., Wolf, S., 2014. Advances and challenges in geotectonic modeling. *Societe Geologique de France* 185, 147–168.

Burov, E., Gerya, T., 2014. Asymmetric three-dimensional topography over mantle plumes. *Nature* 513, 85–103.

Burov, E., Guillou-Frottier, L., 2005. The plume head-lithosphere interaction using a tectonically realistic formulation for the lithosphere. *Geophysical Journal International* 161, 469–490.

Burov, E., Guillou-Frottier, L., d'Acremont, E., Le Pourhiet, L., Cloetingh, S., 2007. Plume head-lithosphere interactions near intra-continental plate boundaries. *Tectonophysics* 434, 15–38.

Burov, E.B., Houdry, F., Diament, M., Déverchère, J., 1994. A broken plate beneath the North Baikal rift zone revealed by gravity modelling. *Geophysical Research Letters* 21 (2), 129–132.

Burov, E., Poliakov, A., 2001. Erosion and rheology controls on syn- and post-rift evolution: verifying old and new ideas using a fully coupled numerical model. *Journal of Geophysical Research* 106, 16461–16481.

Calais, E., et al., 2008. Strain accommodation by slow slip and dyking in a youthful continental rift, East Africa. *Nature* 456, 783–787.

Caristan, Y., 1982. The transition from high temperature creep to fracture in Maryland diabase. *Journal of Geophysical Research* 87, 6781–6790.

Chakrabarti, R., Basu, A.R., Santo, A.P., Tedesco, D., Vaselli, O., 2009. Isotopic and geochemical evidence for a heterogeneous mantle plume origin of the Virunga volcanics, Western rift, East African Rift system. *Chemical Geology* 259, 273–289.

Chang, S.-J., van der Lee, S., 2011. Mantle plumes and associated flow beneath Arabia and East Africa. *Earth and Planetary Science Letters* 302, 448–454.

Chesley, J.T., Rudnick, R.L., Lee, C.T., 1999. Re-Os systematics of mantle xenoliths from the East African Rift: age, structure, and history of the Tanzanian craton. *Geochimica et Cosmochimica Acta* 63, 1203–1217.

Cloetingh, S., Burov, E., Matenco, L., Beekman, F., Roure, F., Ziegler, P., 2013. The Moho in extensional tectonic settings: insights from thermo-mechanical models. *Tectonophysics* 609, 558–604.

Cloetingh, S., Burov, E., Poliakov, A., 1999. Lithosphere folding: primary response to compression? (from central Asia to Paris basin). *Tectonics* 18, 1064–1083.

Chorowicz, J., 2005. The East African rift system. *Journal of African Earth Sciences* 43, 379–410.

Coblentz, D.D., Sandiford, M., 1994. Tectonic stresses in the African plate: constraints on the ambient lithospheric stress state. *Geology* 22, 831–834.

Cohen, A.S., Soreghan, M.J., Scholz, C.A., 1993. Estimating the age of formation of lakes: an example from Lake Tanganyika, East African Rift System. *Geology* 21, 511–514.

Connolly, J.A.D., 2005. Computation of phase equilibria by linear programming: a tool for geodynamic modeling and its application to subduction zone decarbonation. *Earth and Planetary Science Letters* 236, 524–541.

Corti, G., van Wijk, J., Cloetingh, S., Morley, C.K., 2007. Tectonic inheritance and continental rift architecture: numerical and analogue models of the East African Rift system. *Tectonics* 26, TC6006.

Cramer, F., et al., 2012. A comparison of numerical surface topography calculations in geodynamic modelling: an evaluation of the 'sticky air' method. *Geophysical Journal International* 189, 38–54.

Duret, T., May, D.A., Gerya, T.V., Tackley, P.J., 2011. Discretization errors and free surface stabilization in the finite difference and marker-in-cell method for applied geodynamics: a numerical study. *Geochemistry, Geophysics, Geosystems* 12, Q07004.

Durham, W.B., Mei, S., Kohlstedt, D.L., Wang, L., Dixon, N.A., 2009. New measurements of activation volume in olivine under anhydrous conditions. *Physics of the Earth and Planetary Interiors* 172, 67–73.

Ebinger, C.J., 1989. Tectonic development of the western branch of the East African rift system. *Geological Society of America Bulletin* 101, 885–903.

Ebinger, C., Deino, A., Drake, R., Tesha, A., 1989. Chronology of volcanism and rift basin propagation: Rungwe Volcanic Province, East Africa. *Journal of Geophysical Research* 94, 15785–15803.

Ebinger, C.J., Sleep, N., 1998. Cenozoic magmatism throughout East Africa resulting from impact of a single plume. *Nature* 395, 788–791.

Ershov, A.V., Nikishin, A.M., 2004. Recent geodynamics of the Caucasus–Arabia–East Africa region. *Geotectonics* 38, 123–136.

Ferguson, D.J., et al., 2013. Melting during late-stage rifting in Afar is hot and deep. *Nature* 499, 70–73.

- Fitton, J.G., 1983. Active versus passive continental rifting: evidence from the West African rift system. *Tectonophysics* 94, 473–481.
- Foster, A., Ebinger, C., Mbende, E., Rex, D., 1997. Tectonic development of the northern Tanzanian sector of the East African Rift System. *Journal of the Geological Society of London* 154, 689–700.
- Foulger, G.R., et al., 2000. The seismic anomaly beneath Iceland extends down to the mantle transition zone and no deeper. *Geophysical Journal International* 142, F1–F5.
- Foulger, G.R., Hamilton, W.B., 2014. Earth science: plume hypothesis challenged. *Nature* 505, 618.
- Furman, T., 2007. Geochemistry of East African Rift basalts: an overview. *Journal of African Earth Sciences* 48, 147–160.
- Furman, T., Bryce, J., Rooney, T., Hanan, B., Yirgu, G., Ayalew, D., 2006. Heads and tails: 30 million years of the Afar plume, in the Afar Volcanic Province within the East African Rift System. Geological Society, London, Special Publications 259, 95–119.
- George, R., Rogers, N., Kelley, S., 1998. Earliest magmatism in Ethiopia: evidence for two mantle plumes in one flood basalt province. *Geology* 26, 923–926.
- Gerya, T.V., 2010. Introduction to Numerical Geodynamic Modelling. Cambridge University Press, 345 pp.
- Gerya, T.V., Yuen, D.A., 2007. Robust characteristics method for modelling multi-phase visco-elasto-plastic thermo-mechanical problems. *Physics of the Earth and Planetary Interiors* 163, 83–105.
- Grand, S., 2002. Mantle shear-wave tomography and the fate of subducted slabs. *Philosophical Transactions of the Royal Society of London A360*, 2475–2491.
- Gu, Y.J., Dziewonski, A.M., Su, W., Ekström, G., 2001. Models of the mantle shear velocity and discontinuities in the pattern of lateral heterogeneity. *Journal of Geophysical Research* 106, 11169–11199.
- Guillou-Frotier, L., Burov, E., Cloetingh, S., Le Goff, I., Deschamps, Y., Huet, B., Bouchot, V., 2012. Plume-induced dynamic instabilities near cratonic blocks: Implications for P-T-t paths and metallogeny. *Global and Planetary Change* 90–91, 37–50.
- Halldórsson, S.A., Hilton, D.R., Scarsi, P., Abebe, T., Hopp, J., 2014. A common mantle plume source beneath the entire East African Rift system revealed by coupled helium-neon systematics. *Geophysical Research Letters* 41, 2304–2311.
- Hansen, S.E., Nyblade, A.A., Benoit, M.H., 2012. Mantle structure beneath Africa and Arabia from adaptively parameterized P-wave tomography: Implications for the origin of Cenozoic Afro-Arabian tectonism. *Earth and Planetary Science Letters* 319–320, 23–34.
- Hilton, D.R., Halldórsson, S.A., Barry, P.H., Fischer, T.P., de Moor, J.M., Ramirez, C.J., Mangasini, F., Scarsi, P., 2011. Helium isotopes at Rungwe Volcanic province, Tanzania, and the origin of East African Plateau. *Geophysical Research Letters* 38, L21304.
- Huerta, A.D., Nyblade, A.A., Reusch, A.M., 2009. Mantle transition zone structure beneath Kenya and Tanzania: more evidence for a deep-seated thermal upwelling in the mantle. *Geophysical Journal International* 177, 1249–1255.
- Huisman, R.S., Beaumont, C., 2003. Symmetric and asymmetric lithospheric extension: relative effects of frictional-plastic and viscous strain softening. *Journal of Geophysical Research* 108, 2496.
- Huisman, R.S., Beaumont, C., 2007. Roles of lithospheric strain softening and heterogeneity in determining the geometry of rifts and continental margins. In: Karner, G.D., Manatschal, G., Pinheiro, L.M. (Eds.), *Imaging, Mapping and Modelling Continental Lithosphere Extension and Breakup*, 282. Geological Society, London, Special Publications, pp. 107–134.
- Karato, S.I., Wu, P., 1993. Rheology of the upper mantle. *Science* 260, 771–778.
- Kendall, J.M., Stuart, G.W., Ebinger, C.J., Bastow, I.D., Keir, D., 2005. Magma-assisted rifting in Ethiopia. *Nature* 433, 146–148.
- Kendall, J.-M., Pilidou, S., Keir, D., Bastow, I.D., Stuart, G.W., Ayele, A., 2006. Mantle upwellings, melt migration and the rifting of Africa: insights from seismic anisotropy. In: Yirgu, G., Ebinger, C.J., Maguire, P.K.H. (Eds.), *The Afar Volcanic Province within the East African Rift System*, 259. Geological Society, London, Special Publications, pp. 55–72.
- Koptev, A., Calais, E., Burov, E., Leroy, S., Gerya, T., 2015. Dual continental rift systems generated by plume–lithosphere interaction. *Nature Geoscience* 8, 388–392.
- Lee, C.-T., Rudnick, R.L., 1999. Compositionally stratified cratonic lithosphere: petrology and geochemistry of peridotite xenoliths from the Labait volcano, Tanzania. In: Gurney, J., Gurney, J., Pascoe, M., Richardson, S. (Eds.), *Proceedings of the 7th International Kimberlite Conference. Red Roof Design cc, Cape Town*, pp. 503–521.
- Lezzar, K.E., Tiercelin, J.J., De Batist, M., Cohen, A.S., Bandora, T., van Resbergen, P., Le Turdu, C., Mifundu, W., Klerkx, J., 1996. New seismic stratigraphy and late Tertiary history of the North Tanganyika basin, East African rift system, deduced from multichannel and high-resolution reflection seismic data and piston core evidence. *Basin Research* 8, 1–28.
- Lin, S.-C., Kuo, B.-Y., Chiao, L.-Y., van Keken, P.E., 2005. Thermal plume models and melt generation in East Africa: a dynamic modeling approach. *Earth and Planetary Science Letters* 237, 175–192.
- Lithgow-Bertelloni, C., Silver, P.G., 1998. Dynamic topography, plate driving forces and the African superswell. *Nature* 395, 269–272.
- Logatchev, N.A., Belousov, V.V., Milanovsky, E.E., 1972. East African rift development. *Tectonophysics* 15 (1), 71–81.
- MacDonald, R., Rogers, N.W., Fitton, J.G., Black, S., Smith, M., 2001. Plume_lithosphere interactions in the generation of the basalts of the Kenya Rift, East Africa. *Journal of Petrology* 42, 877–900.
- Masters, T.G., Laske, G., Bolton, H., Dziewonski, A., 2000. The relative behavior of shear velocity, bulk sound speed, and compressional velocity in the mantle: implications for chemical thermal structure, in Earth's deep interior: mineral physics and tomography from the atomic to the global scale. *Geophysical Monograph* 117, 63–87.
- McConnell, R.B., 1972. Geological development of the rift system of eastern Africa. *Geological Society of America Bulletin* 83, 2549–2572.
- McDougall, I., Brown, F.H., 2009. Timing of volcanism and evolution of the northern Kenya Rift. *Geological Magazine* 146, 34–47.
- McKenzie, D., 1978. Some remarks on the development of sedimentary basins. *Earth and Planetary Science Letters* 40, 25–32.
- Mégnin, C., Romanowicz, B., 2000. The three-dimensional shear velocity structure of the mantle from the inversion of body, surface, and higher-mode waveforms. *Geophysical Journal International* 143, 709–728.
- Mohr, P., 1982. Musings on continental rifts. In: Palmason, G. (Ed.), *Continental and Oceanic Rifts, American Geophysical Union Geodynamics Series*, 8, pp. 293–309.
- Morley, C.K., 1988. Variable extension in Lake Tanganyika. *Tectonics* 7, 785–801.
- Morley, C.K., et al., 1992. Tectonic evolution of the northern Kenyan Rift. *Journal of the Geological Society* 149, 333–348.
- Moucha, R., Forte, A.M., 2011. Changes in African topography driven by mantle convection. *Nature Geoscience* 4, 707–712.
- Mulibo, G.D., Nyblade, A.A., 2013a. The P and S wave velocity structure of the mantle beneath eastern Africa and the African superplume anomaly. *Geochemistry, Geophysics, Geosystems* 14, 2696–2715.
- Mulibo, G.D., Nyblade, A.A., 2013b. Mantle transition zone thinning beneath eastern Africa: evidence for a whole-mantle superplume structure. *Geophysical Research Letters* 40, 3562–3566.
- Nelson, W.R., Furman, T., Hanan, B., 2008. Sr, Nd, Pb, and Hf evidence for two-plume mixing beneath the East African Rift system. *Geochimica et Cosmochimica Acta* 72, A676.
- Nelson, W.R., Furman, T., van Keken, P.E., Shirey, S.B., Hanan, B.B., 2012. Os-Hf isotopic insight into mantle plume dynamics beneath the East African Rift System. *Chemical Geology* 320–321, 66–79.
- Nolet, G., Richard, A., Zhao, D., 2007. Mantle plume tomography. *Chemical Geology* 241, 248–263.
- Nolet, G., Karato, S.-I., Montelli, R., 2006. Plume fluxes from seismic tomography. *Earth and Planetary Science Letters* 248, 685–699.
- Nyblade, A.A., 1997. Heat flow across the East African plateau. *Geophysical Research Letters* 24, 2083–2086.
- Nyblade, A.A., 2011. The upper-mantle low-velocity anomaly beneath Ethiopia, Kenya, and Tanzania: constraints on the origin of the African superswell in eastern Africa and plate versus plume models of mantle dynamics. *The Geological Society of America Special Paper* 478, 1–14.
- Nyblade, A.A., Brazier, R.A., 2002. Precambrian lithospheric controls on the development of the East African Rift system. *Geology* 30, 755–758.
- Nyblade, A.A., Owens, T.J., Gurrilla, H., Ritsema, J., Langston, C.A., 2000. Seismic evidence for a deep upper mantle thermal anomaly beneath east Africa. *Geology* 28, 599–602.
- Olson, P., Schubert, G., Turcotte, D., 2001. *Mantle Convection in the Earth and Planets*. Cambridge University Press, 940pp.
- Petit, C., Burov, E.B., Déverchère, J., 1997. On the structure and the mechanical behaviour of the extending lithosphere in the Baikal Rift from gravity modeling. *Earth and Planetary Science Letters* 149, 29–42.
- Petit, C., Ebinger, C.J., 2000. Flexure and mechanical behavior of cratonic lithosphere: gravity models of the East African and Baikal rifts. *Journal of Geophysical Research* 105, 19151–19162.
- Pik, R., Marty, B., Hilton, D.R., 2006. How many mantle plumes in Africa? The geochemical point of view. *Chemical Geology* 226, 100–114.
- Precigout, J., Gueydan, F., Gapais, D., Garrido, C., Essaifi, A., 2007. Strain localisation in the subcontinental mantle: a ductile alternative to the brittle mantle. *Tectonophysics* 445, 318–336.
- Ring, U., 1994. The influence of preexisting structure on the evolution of the Cenozoic Malawi Rift (East African Rift system). *Tectonics* 13, 313–326.
- Ritsema, J., Nyblade, A.A., Owens, T.J., Langston, C.A., 1998. Upper mantle seismic velocity structure beneath Tanzania, East Africa: Implications for the stability of cratonic lithosphere. *Journal of Geophysical Research* 103, 21201–21213.
- Ritsema, J., van Heijst, H.J., Woodhouse, J.H., 1999. Complex shear wave velocity structure imaged beneath Africa and Iceland. *Science* 286, 1925–1928.
- Ritsema, J., Deuss, A., van Heijst, H.J., Woodhouse, J.H., 2011. S40RTS: a degree-40 shear velocity model for the mantle from new Rayleigh wave dispersion, teleseismic traveltimes and normal-mode splitting function measurements. *Geophysical Journal International* 184, 1223–1236.
- Roberts, E.M., et al., 2012. Initiation of the western branch of the East African Rift coeval with the eastern branch. *Nature Geoscience* 5, 289–294.
- Rogers, N., MacDonald, R., Fitton, J.G., George, R., Smith, M., Barreiro, B., 2000. Two mantle plumes beneath the East African rift system: Sr, Nd and Pb isotope evidence from Kenya Rift basalts. *Earth and Planetary Science Letters* 176, 387–400.
- Rooney, T.O., Herzberg, C., Bastow, I.D., 2012. Elevated mantle temperature beneath East Africa. *Geology* 40, 27–30.
- Saria, E., Calais, E., Stamps, D.S., Delvaux, D., Hartnady, C.J.H., 2014. Present-day kinematics of the East African Rift. *Journal of Geophysical Research* 119, 3584–3600.

- Satsukawa, T., et al., 2011. Seismic anisotropy of the uppermost mantle beneath the Rio Grande rift: evidence from Kilbourne Hole peridotite xenoliths, New Mexico. *Earth and Planetary Science Letters* 311, 172–181.
- Sengör, A.M.C., Burke, K., 1978. Relative timing of rifting and volcanism on Earth and its tectonic implications. *Geophysical Research Letters* 5, 419–421.
- Simmons, N.A., Myers, S.C., Johannesson, G., 2011. Global-scale P wave tomography optimized for prediction of teleseismic and regional travel times for Middle East events: 2. Tomographic inversion. *Journal of Geophysical Research* 116, 257–265.
- Sleep, N.H., Ebinger, C.J., Kendall, J.M., 2002. Deflection of mantle plume material by cratonic keels. *Geological Society, London, Special Publications* 199, 135–150.
- Smith, M., 1994. Stratigraphic and structural constraints on mechanisms of active rifting in the Gregory Rift, Kenya. *Tectonophysics* 236, 3–22.
- Spath, A., Le Roex, A.P., Opiyo-Akech, N., 2001. Plume-lithosphere interaction and the origin of continental rift-related alkaline volcanism, the Chyulu Hills Volcanic Province, southern Kenya. *Journal of Petrology* 42, 765–787.
- Stab, M., Bellahsen, N., Pik, R., Quidelleur, X., Ayalew, D., Leroy, S., 2015. Mode of rifting in magma-rich settings: Tectono-magmatic evolution of Central Afar. *Tectonics*. <http://dx.doi.org/10.1002/2015TC003893>.
- Stamps, D.S., et al., 2008. A kinematic model for the East African Rift. *Geophysical Research Letters* 35, L05304.
- Stamps, D.S., Flesch, L.M., Calais, E., 2010. Lithospheric buoyancy in Africa from a thin sheet approach. *International Journal of Earth Sciences* 99, 1525–1533.
- Stamps, D.S., Flesch, L.M., Calais, E., Ghosh, A., 2014. Current kinematics and dynamics of Africa and the East African Rift System. *Journal of Geophysical Research: Solid Earth* 119, 5161–5186.
- Stamps, D.S., Iaffaldano, G., Calais, E., 2015. Role of mantle flow in Nubia-Somalia plate divergence. *Geophysical Research Letters* 42, 290–296.
- Tiercelin, J.J., Lezzar, K.E., Odada, E.O., Olago, D.O. (Eds.), 2002. *The East African Great Lakes: Limnology, Palaeolimnology and Biodiversity*, 3–60. Kluwer Academic.
- Venkataraman, A., Nyblade, A.A., Ritsema, J., 2004. Upper mantle Q and thermal structure beneath Tanzania, East Africa from teleseismic P wave spectra. *Geophysical Research Letters* 31, L15611.
- Versfelt, J., Rosendahl, B.R., 1989. Relationships between pre-rift structure and rift architecture in lakes Tanganyika and Malawi: East Africa. *Nature* 337, 354–357.
- Watremez, L., Burov, E., d'Acremont, E., Leroy, S., Huet, B., Le Pourhiet, L., Bellahsen, N., 2013. Buoyancy and localizing properties of continental mantle lithosphere: Insights from thermomechanical models of the eastern Gulf of Aden. *Geochemistry, Geophysics, Geosystems* 14 (8), 2800–2817.
- Weeraratne, D.S., Forsyth, D.W., Fischer, K.M., Nyblade, A.A., 2003. Evidence for an upper mantle plume beneath the Tanzanian craton from Rayleigh wave tomography. *Journal of Geophysical Research* 108 (B9), 2427.
- Whitmarsh, R.B., Manatschal, G., Minshull, T.A., 2001. Evolution of magma-poor continental margins from rifting to seafloor spreading. *Nature* 413, 150–154.
- Wichura, H., Bousquet, R., Oberhansli, R., Strecker, M.R., Trauth, M.H., 2011. The Mid-Miocene East African Plateau: a pre-rift topographic model inferred from the emplacement of the phonolitic Yatta lava flow, Kenya. *Geological Society, London, Special Publications* 357, 285–300.
- Wolfenden, E., Ebinger, C., Yirgu, G., Deino, A., Ayalew, D., 2004. Evolution of the northern Main Ethiopian Rift: birth of a triple junction. *Earth and Planetary Science Letters* 224, 213–228.
- Yang, Z., Chen, W.P., 2010. Earthquakes along the East African Rift system: a multiscale, system-wide perspective. *Journal of Geophysical Research* 115, B12309.
- Yuen, D.A., Monnereau, M., Hansen, U., Kameyama, M., Matyska, C., 2007. Dynamics of superplumes in the lower mantle. In: Yuen, D.A., Maruyama, S., Karato, S., Windley, B.F. (Eds.), *Superplumes: Beyond Plate Tectonics*. Springer Verlag, Heidelberg, pp. 239–268.
- Zeyen, H., Volker, F., Wehrle, V., Fuchs, K., Sobolev, S.V., Altherr, R., 1997. Styles of continental rifting: crust-mantle detachment and mantle plumes. *Tectonophysics* 278, 329–352.



Alexander Koptev is a post-doctoral researcher at University of Pierre and Marie Curie (Paris VI). After his M.Sc in Geology (2008) from the Geological Department of Lomonosov Moscow State University, Russia, he started to work on geophysical processes in the Earth interior and completed his Ph.D from the same University in 2011. At present time, he is a member of ISTEP (the Institute of Earth Sciences of Paris) research group and his research is primarily focused on plume-lithosphere interactions and continental rift formation and, more broadly, numerical modeling of geodynamical processes.



Evgueni Burov is a professor at the Institute of Earth Sciences of Paris (ISTEP) of the University of Pierre and Marie Curie. His work has a special focus on concepts in long-term lithosphere rheology, the mechanisms of intra-plate deformation, such as plate bending, mountain building and basin formation. He established quantitative links between observations of flexural deformation of the continental lithosphere and its non-linear rheology and multi-layer structure. He has also studied the interplays of mantle flow and plumes and lithosphere deformation, and the links between short-term and long-term deformation in the lithosphere. His work is also devoted to implementation of new conceptual and methodological approaches for frontier thermo-mechanical numerical models capable of handling strong non-linear rheologies, surface processes, and large strain tectonic deformation. He was awarded Stephan Mueller Medal of European Geosciences Union in 2015.



Eric Calais is a professor and Head of the Geosciences Department at the Ecole Normale Supérieure in Paris, France. His research focuses on the kinematics and dynamics of active tectonic processes which he studies by combining observations from space geodesy and models of lithospheric deformation. He initiated and led field experiments in the Caribbean, central Asia, and east Africa to study active deformation processes at spatial and temporal scales ranging from individual earthquakes or volcanic events to the deformation of plate margins. His is also involved in research on large earthquakes in intraplate regions such as the Central Eastern U.S. and western Europe. He was science advisor for the United Nations in 2010–2012 in the aftermath of the Haiti earthquake.



Sylvie Leroy is a researcher at the Institute of Earth Sciences of Paris (ISTEP) of the University of Pierre and Marie Curie. She uses multichannel seismic and active-source seismology together with other geophysical (heat flow, seismology etc.) and geological data to investigate deformation and magmatism at plate boundaries, including continental rifts and rifted margins, ocean-continent transition, spreading ridges and transforms.



Taras Gerya is a professor at the Swiss Federal Institute of Technology (ETH-Zurich) working in the field of numerical modeling of geodynamic and planetary processes. He received his undergraduate training in Geology at the Tomsk Polytechnic Institute, his Ph.D. in Petrology at the Moscow State University and his Habilitation in Geodynamics at ETH-Zurich. His present research interests include subduction and collision processes, ridge-transform oceanic spreading patterns, plume-lithosphere interactions, generation of earthquakes, fluid and melt transport in the lithosphere, Precambrian geodynamics and core and surface formation of terrestrial planets. He is the author of *Introduction to Numerical Geodynamic Modeling* (Cambridge University Press, 2010).



Laurent Guillou-Frottier is a research engineer at the Bureau de Recherches Géologiques et Minières (BRGM, the French Geological Survey) working mainly in the fields of mineral resources and geothermics. After undergraduate diplomas in Earth Sciences and Applied Physics at University Pierre et Marie Curie and University Paris Diderot, he received his PhD and his Habilitation in Geophysics at the Institut de Physique du Globe de Paris (IPGP). His recent research interests include the role of subduction-related processes in the emplacement of porphyry-copper deposits, the role of mantle plumes in metallogenic crises, the occurrence of hydrothermal processes during weathering of ultramafic rocks, and the establishment of thermal anomalies in sedimentary basins.



Sierd Cloetingh is Royal Netherlands Academy Professor of Earth Sciences at Utrecht University. He published more than 300 papers in international peer-reviewed journals and has been promotor of more than 70 PhD students of 18 different nationalities. He served the Earth Science community in various functions, including Presidency of the European Geophysical Society. He is currently the President of the International Lithosphere Programme, Editor-in-Chief of the International Journal "Global and Planetary Change" and Chairman of the Scientific Committee of the ESF Large Scale Collaborative Research Programme (EUROCORES) TOPO-EUROPE. He received honorary doctorates from five European universities and numerous honors

and awards, including the Stephan Mueller Medal, Arthur Holmes Medal and honorary membership of the European Geosciences Union, Fellow and Honorary Fellow of the American Geophysical Union and the Geological Society of America, the Leopold von Buch Medal of the German Geological Society and the Alexander von Humboldt Research Award. He is member of the Royal Netherlands Academy of Arts and Sciences and Foreign member of the Royal Norwegian Academy of Sciences, the Royal Danish Academy of Sciences, the Heidelberg Academy, the Bavarian Academy and the German Academy for Technical Sciences, Acatech. He was distinguished in 2006 as Chevalier de Legion d'Honneur and in 2014 as Knight of the Royal Order of the Netherlands Lion for his contributions to science and European scientific cooperation in research and education. He was elected member of Academia Europaea in 1994 and served Academia Europaea as Chair of the Earth and Marine and Earth and Cosmic Sciences Sections and as Vice-President. In 2014 he was elected as President of Academia Europaea. He is a member of the Scientific Council of the ERC since 2009. In 2015 he was appointed as Vice-President of the ERC and coordinator of the ERC domain Physical Sciences and Engineering (PE).